Eurasian Journal of Physics and Functional Materials

2026, 10(2), 178-189

WO_3 nanopowders as efficient photocatalysts for paracetamol degradation

G.Zh. Assilbekova[1,2], A.A. Markhabayeva[1,2,3,*], R.R. Nemkayeva[1,2,3], B.Ye. Zhumadilov[1,2,3], R.Ye. Zhumadilov[1,2,3], N.Ye. Akhanova[1,3], G.A. Kaliyeva[4], M.T. Gabdullin[1,3], Ye. Yerlanuly[1,3,5*]

[1]Institute of Applied Science and Information Technologies, Almaty, Kazakhstan

[2]Al Farabi Kazakh National University, Almaty, Kazakhstan

[3]Kazakh-British Technical University, Almaty, Kazakhstan

[4]School-Lyceum 131 named after B. Momyshuly, Almaty, Kazakhstan

[5]Central Asian Institute of Advanced Science, Almaty, Kazakhstan

E-mail: yerlanuly@physics.kz, ayymkul.markhabaeva@kaznu.kz

DOI: **10.32523/ejpfm.2026100206**
Received: 06.05.2026 - after revision

The photocatalytic degradation of paracetamol, a widely detected pharmaceutical contaminant, was investigated using WO_3 nanopowders synthesized via a hydrothermal method. The obtained materials exhibited a hierarchical micro/nanostructured morphology composed of interconnected grains and well-defined nanoplate-like particles. Optical characterization revealed an indirect band gap of approximately 2.9 eV. The photocatalytic performance of WO_3 was evaluated under light irradiation, demonstrating a gradual decrease in paracetamol concentration with increasing irradiation time. The degradation process followed pseudo-first-order kinetics, with an apparent rate constant (k_{app}) of 2.54×10^{-2} min^{-1} . The enhanced photocatalytic activity is attributed to the developed surface morphology and improved charge transport within the interconnected structure. These results highlight the potential of WO_3 nanopowders as effective photocatalysts for the removal of pharmaceutical pollutants from aqueous environments.

Keywords: photocatalysis; nanopowders; paracetamol; pharmaceutical pollutants; kinetics; water treatment

Introduction

Pharmaceutical contaminants have emerged as a significant class of environmental pollutants due to their widespread use and continuous release into aquatic systems. Among them, paracetamol (acetaminophen) is one of the most commonly consumed analgesic and antipyretic drugs, frequently detected in wastewater and natural water bodies. Its incomplete removal in conventional treatment processes raises concerns regarding its persistence and potential ecological impact. Moreover, paracetamol exhibits moderate resistance to biological degradation and may lead to the formation of harmful intermediate products during partial oxidation [1–4].

Advanced oxidation processes, particularly semiconductor-based photocatalysis, have attracted considerable attention as efficient and environmentally friendly methods for the degradation of pharmaceutical pollutants. Photocatalysis enables the generation of reactive oxygen species under light irradiation, leading to the mineralization of organic contaminants [5,6]. Among various photocatalytic materials, tungsten oxide (WO_3) has been widely investigated due to its suitable band gap, good chemical stability, and strong absorption in the visible region. In addition, the photocatalytic performance of WO_3 is strongly influenced by its morphology, particle size, and surface structure, which affect light absorption, charge separation, and the availability of active sites [7–11]. Despite extensive research on WO_3 -based photocatalysts, a comprehensive understanding of the relationship between synthesis conditions, resulting morphology, and photocatalytic performance in the degradation of pharmaceutical compounds remains limited [12].

In this work, WO_3 nanopowders were synthesized via a hydrothermal method and applied for the photocatalytic degradation of paracetamol under light irradiation. The influence of morphology and optical properties on photocatalytic activity was systematically investigated. Special attention was devoted to the analysis of degradation kinetics, which were found to follow a pseudo-first-order model based on the Langmuir–Hinshelwood mechanism. The results of this study provide insights into the design of efficient WO_3 -based photocatalysts for wastewater treatment and environmental remediation.

Material and methods

Photocatalyst preparation

Chemicals: Distilled water with a resistivity of 18 $M\Omega \cdot cm$, obtained from an ELGA Purelab or ARIUM 611 DI water purification system, was used in all experiments. Sodium tungstate dihydrate ($Na_2WO_4 \cdot 2H_2O$, $>$ 99%, Sigma-Aldrich) and ammonium tungstate (ACS reagent, $>$ 99%, Sigma-Aldrich) were employed as tungsten precursors for the synthesis of tungsten oxide nanopowders. Citric acid and nitric acid (98%, Acros Organics) were used as chelating and pH-adjusting agents without further purification.

Synthesis of WO_3 nanopowders. For the hydrothermal synthesis of tungsten oxide powders, an aqueous solution containing 0.08 M sodium tungstate dihydrate ($Na_2WO_4 \cdot 2H_2O$) and 0.1 M citric acid was prepared. The solution was stirred at room temperature for 1 h to ensure complete complexation of tungsten species. Citric acid acted as a chelating agent, stabilizing tungstate ions in solution and controlling the nucleation and growth of tungsten oxide particles. Subsequently, hydrochloric acid (HCl, 5 M) was added dropwise to adjust the solution acidity to pH = 1.5. The addition of HCl induced protonation of tungstate species and promoted the formation of tungstic acid precursors, triggering the condensation and crystallization processes. As-prepared precursor solution was transferred into a Teflon-lined stainless-steel autoclave for hydrothermal treatment at elevated temperature. Approximately 50 mL of the growth solution was poured into a 50 mL Teflon vessel, which was then placed inside a stainless-steel autoclave and hermetically sealed. The autoclave was subsequently introduced into a muffle furnace preheated to the synthesis temperature, where hydrothermal synthesis was carried out at 180 °C for 4 h. After completion of the reaction, the autoclave was allowed to cool naturally to room temperature. The obtained suspension was washed several times with distilled water to remove residual ions and by-products, followed by drying at 90 °C in air for approximately 12 h.

Photocatalytic activity evaluation

Photocatalytic experiments were carried out using an aqueous solution of paracetamol. A known amount of photocatalyst was dispersed in the solution and stirred in the dark for 30 min to establish adsorption–desorption equilibrium. Subsequently, the suspension was irradiated with UV–visible light under continuous stirring. At regular time intervals, aliquots were collected, centrifuged to remove the catalyst, and analyzed by UV–Vis spectroscopy. The degradation efficiency was calculated using the relation: $\eta = (C_0 - C)/C_0 \times 100\%$, where C_0 and C are the initial and remaining dye concentrations, respectively. The photocatalytic kinetics were analyzed using a pseudo-first-order model according to the Langmuir–Hinshelwood mechanism: $\ln(C_0/C_t) = kt$, where k is rate constant, C_0 is the initial concentration and C_t is the concentration at time t.

Characterization techniques

Sample morphology was examined using scanning electron microscopy (SEM, ZEISS Crossbeam 540). Structural ordering and vibrational properties of the materials were characterized by Raman spectroscopy (Solver Spectrum NT-MDT, 473 nm excitation), while crystalline phases and lattice structure were identified via X-ray diffraction (XRD, Rigaku SmartLab, Cu Kα radiation, $\lambda = 1.5406$ Å).

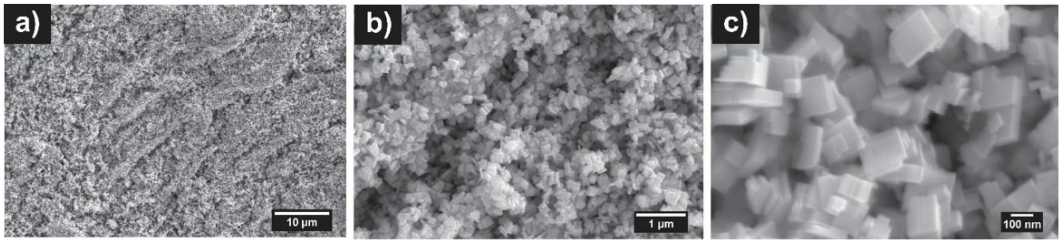

Figure 1. SEM images of WO_3 powders at different magnifications: (a) low-magnification overview showing agglomerated microstructured surface (scale bar 10 μ m); (b) intermediate magnification revealing densely packed micro-grains (scale bar 1 μ m); (c) high-magnification image showing well-defined nanoblock/nanoplate-like particles with sizes in the range of $\sim$ 80–150 nm (scale bar 100 nm).

Results and Discussion

The morphology of the WO_3 powders was examined by scanning electron microscopy (SEM) (Figure 1). At low magnification (Figure 1a), the sample exhibits a highly agglomerated microstructured surface composed of irregular clusters distributed over several micrometers. At higher magnification (Figure 1b), the structure is resolved into densely packed micro-grains forming a porous network. The grains appear interconnected, which may facilitate charge transport and improve accessibility of reactive sites during photocatalytic processes. The high-magnification image (Figure 1c) reveals that the material consists of well-defined nanoblock or nanoplate-like particles with characteristic lateral dimensions in the range of approximately 80–150 nm. The relatively uniform particle size distribution and the presence of sharp edges indicate good crystallization of the WO_3 phase. Such hierarchical micro/nanostructured morphology is beneficial for photocatalytic applications, as it increases the effective surface area and enhances light harvesting due to multiple scattering within the agglomerated structure.

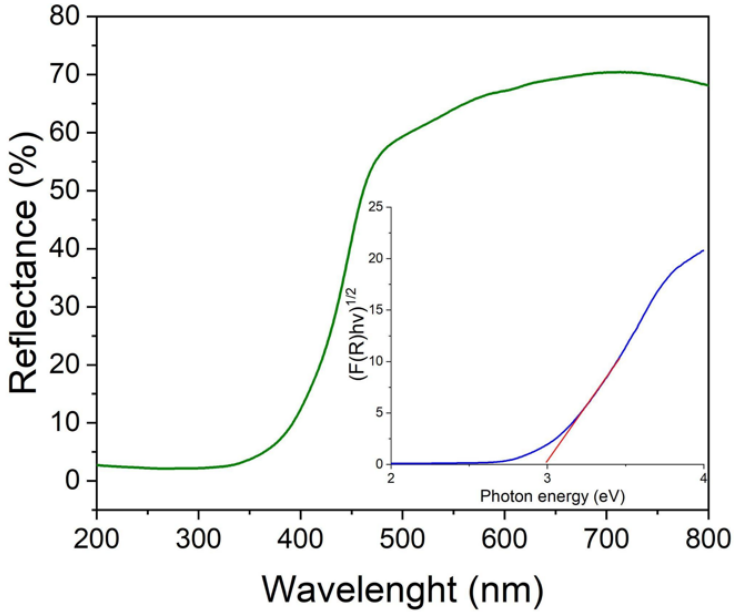

Figure 2. UV–Vis diffuse reflectance spectrum of WO_3 powders and the corresponding Tauc plot (insert) derived using the Kubelka–Munk function.

The optical band gap was estimated from the Tauc plot using the Kubelka–Munk transformation (Figure 2). The extrapolation of the linear region of $h\nu$

yields an indirect band gap of approximately $\sim$2.9 eV, corresponding with other works [13,14]. The absorption edge located around 400–450 nm indicates that WO_3 can be activated under near UV and partially visible light irradiation. Additionally, slight tailing of the absorption edge may be attributed to defect states such as oxygen vacancies, which can improve charge separation and enhance photocatalytic performance.

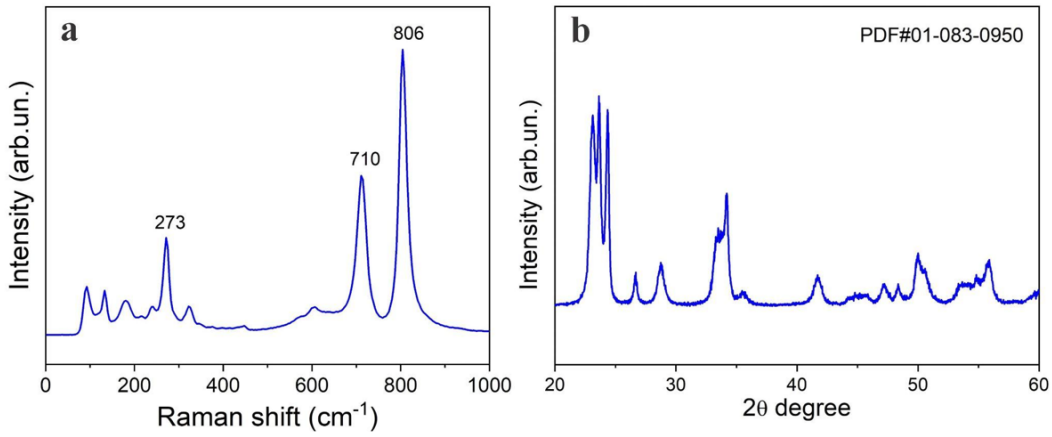

Figure 3. (a) Raman spectrum and (b) XRD pattern of WO_3 nanopowders.

The structural properties of the WO_3 powders were characterized by Raman spectroscopy (Figure 3a). The spectrum recorded in the range of 50–1000 cm $^{-1}$ exhibits characteristic bands consistent with the monoclinic phase of WO_3. The two most prominent bands, located at 710 cm $^{-1}$ and 806 cm $^{-1}$, are assigned to symmetric stretching vibrations of bridging O–W–O bonds. The band at 273 cm $^{-1}$ is attributed to bending vibrations of O–W–O bond [15–17]. The well-defined nature of these bands indicates a high degree of crystallinity of the WO_3 sample. The positions and relative intensities of all observed bands are in good agreement with previously reported data for monoclinic WO_3. The Raman peak parameters are summarized in Table 1.

Table 1.
Parameters of Raman peaks for WO_3.

	Ti/WO_3	FWHM (cm^{-1})	I (intensity)
O–W–O bending	273	12.8	2335
O–W–O stretching	710	19.7	3724
O–W–O stretching	806	18.3	6547

The crystal structure of the WO_3 powders was examined by X-ray diffraction (XRD). The diffraction pattern (Figure 3b, Table 2) reveals a set of sharp and well-resolved reflections that are fully indexed within the monoclinic WO_3 structure and are in good agreement with the reference card PDF#01-083-0950. The most intense peaks are observed in the 2θ range of approximately 23–25 °, corresponding to the (002), (020), and (200) crystallographic planes. Additional reflections are detected at 2θ = 26.7, 28.7, 33.2, 34.2 and 35.5, which can be assigned to the (120), (112), (022), (202) and (122) planes, respectively [18–21]. The observed set of diffraction maxima is fully consistent with the standard pattern

for monoclinic WO_3. The strongest diffraction peak observed at $2\theta = 23.6^\circ$, corresponding to the (020) reflection, indicates a preferential growth of WO_3 crystallites in the (020) direction. To determine the average crystallite size, the peak broadening was analyzed using the Scherrer equation, $D = K\lambda/(\beta\cos\theta)$, in which K represents the shape factor (0.9), λ denotes the X-ray wavelength (1.5406 Å), β is the full width at half maximum (FWHM) expressed in radians, and θ is the Bragg diffraction angle. Based on this analysis, the crystallite size derived from the (020) reflection was found to be ~ 25 nm.

Table 2.
Parameters of XRD for WO_3.

Crystal planes	WO_3
(002)	23.1
(020)	23.6
(200)	24.3
(120)	26.7
(112)	28.7
(022)	33.2
(202)	34.2
(122)	35.5
(222)	41.7
(004)	47.2
(040)	48.3
(400)	50
(114)	50.5
(024)	53.6

Overall, the combination of Raman spectroscopy and XRD analysis demonstrates a high degree of structural ordering of the synthesized WO_3 powders. The presence of sharp and intense Raman-active vibrational modes together with well-defined and narrow XRD reflections confirms the formation of a highly crystalline monoclinic WO_3 phase with good long-range structural order and low defect concentration.

Figure 4 presents the full UV–Vis absorption spectra recorded during the photocatalytic degradation of paracetamol at a concentration of 50 mg/L using WO_3 powders as the photocatalyst. A progressive attenuation of the characteristic absorption peak at 243 nm was observed with increasing irradiation time, demonstrating the effective photocatalytic decomposition of paracetamol under the applied experimental conditions [22]. The continuous attenuation of this peak without the emergence of new distinct absorption bands suggests that the process is governed by photocatalytic degradation rather than simple adsorption. Under light irradiation, WO_3 generates electron–hole pairs that lead to the formation of reactive oxygen species, which are responsible for the oxidative degradation of paracetamol [18]. These results demonstrate the strong photocatalytic performance of WO_3 powders and their potential application in environmental remediation.

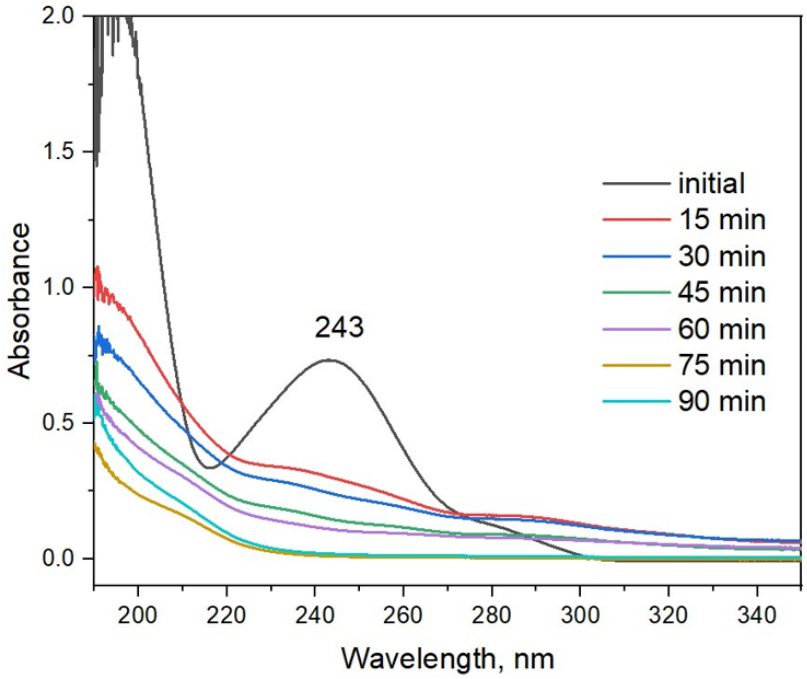

Figure 4. Photocatalytic degradation of paracetamol in the presence of WO_3 -based powders under light irradiation. The normalized concentration (C/C_0) as a function of irradiation time demonstrates the degradation efficiency of the catalyst.

The hydrothermal synthesis conditions, particularly the temperature (180 °C), reaction duration (4 h), and the use of citric acid as a chelating agent, play a decisive role in determining the structural, optical, and electronic properties of the resulting WO_3 nanopowders. The controlled nucleation and growth promoted by citric acid complexation, combined with the acidic environment (pH = 1.5), favors the formation of well-crystallized monoclinic WO_3 with a nanoplate-like morphology. The high crystallinity confirmed by XRD and Raman spectroscopy results in a well-defined band structure with an optical band gap of $\sim$2.9 eV.

The linear relationship between $\ln(C/C_0)$ and irradiation time, as illustrated in Figure 5, confirms that the photodegradation of paracetamol follows pseudo-first-order kinetics within the Langmuir–Hinshelwood model [23]. The high correlation coefficient ($R^2 = 0.979$) indicates an excellent agreement with the kinetic model. The apparent rate constant ($k_{app} = 2.54 \times 10^{-2}$ min $^{-1}$) demonstrates the efficient photocatalytic activity of the WO_3 nanopowders. This performance can be attributed to the effective generation of reactive oxygen species and improved charge separation under light irradiation. According to the Langmuir–Hinshelwood mechanism, the degradation process involves adsorption of paracetamol molecules onto the catalyst surface followed by their oxidation. Minor deviations observed at the initial stage may be related to the establishment of adsorption–desorption equilibrium. Overall, the obtained rate constant is comparable to or exceeds values reported for similar WO_3 -based systems, highlighting the promising potential of the synthesized material for wastewater treatment applications.

The stability and reusability of the WO_3 nanopowders were evaluated through three consecutive photocatalytic degradation cycles under identical experimental conditions. As shown in Figure 6, the photocatalytic activity remains relatively

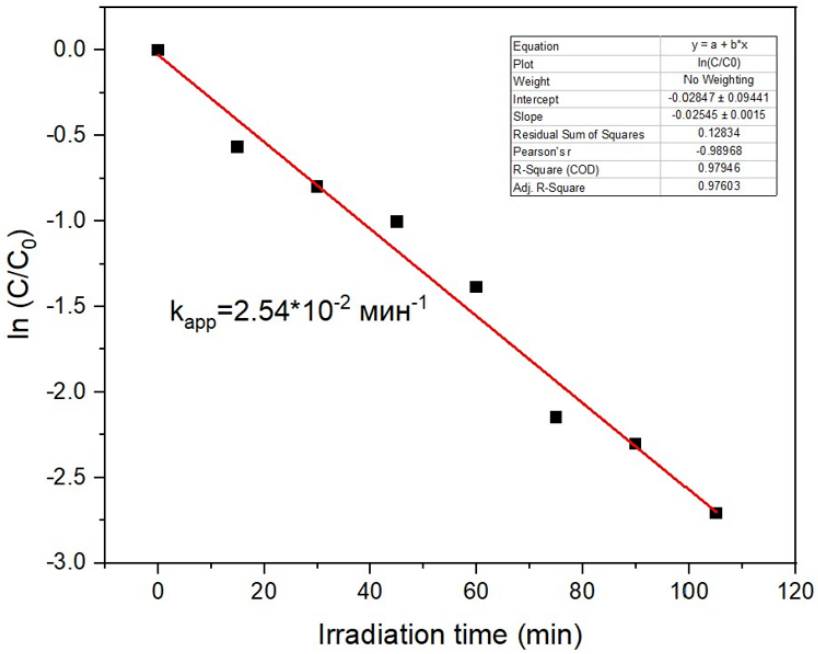

Figure 5. Pseudo-first-order kinetic plot for the photocatalytic degradation of paracetamol over WO_3 -based powders under light irradiation.

stable with only a slight decrease after repeated use. After 90 min of irradiation, the degradation efficiencies remained above 85% for all cycles, indicating good photocatalytic stability of the synthesized WO_3 nanopowders. The minor reduction in activity after repeated cycling may be associated with partial surface adsorption of intermediate products or slight catalyst loss during washing and recovery processes. Overall, the obtained results demonstrate that the synthesized WO_3 powders possess good reusability and structural stability, highlighting their potential for practical wastewater treatment applications.

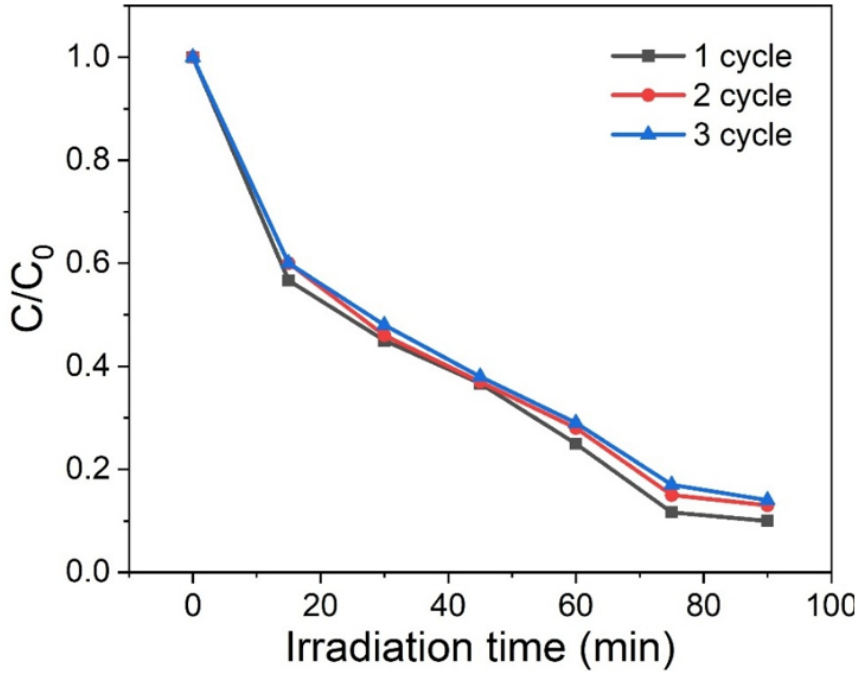

Figure 6. Reusability and stability of WO_3 nanopowders during repeated photocatalytic degradation of paracetamol under UV–visible light irradiation.

To evaluate the structural stability of the WO_3 nanopowders after photocatalytic reaction, Raman spectra were recorded before and after photocatalysis (Figure 7). The characteristic Raman bands of monoclinic WO_3 remain clearly visible after the experiment, confirming preservation of the main crystal structure. A slight shift and broadening of several Raman bands can be observed after photocatalysis, which may be associated with minor surface modification, adsorbed reaction intermediates, or changes in defect concentration during irradiation. However, no new Raman bands corresponding to secondary phases or decomposition products appear, indicating that the WO_3 nanopowders retain their structural integrity during the photocatalytic process.

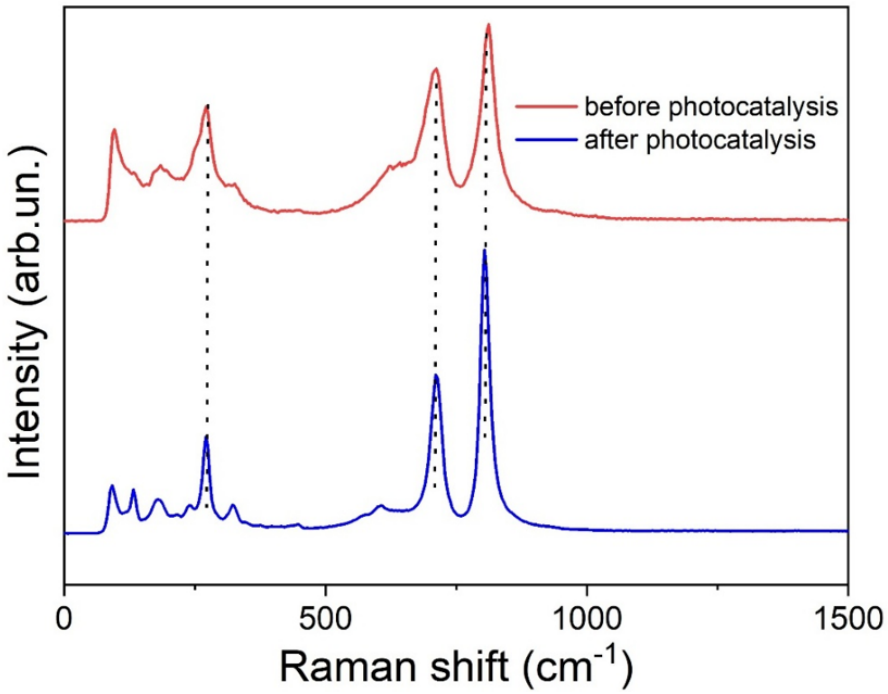

Figure 7. Raman spectra of WO_3 nanopowders before and after photocatalytic degradation experiments, demonstrating preservation of the monoclinic WO_3 structure after repeated use.

To evaluate the photocatalytic performance of WO_3 nanopowders in the present study, a comparative analysis was carried out considering key parameters such as synthesis method, morphology, degradation rate, and light source. The results are summarized in Table 3, which presents previously reported data on the photocatalytic degradation of paracetamol using various WO_3-based and composite photocatalysts. Although such comparisons are inherently relative due to variations in experimental conditions including catalyst dosage, light source type, irradiation power (W), reaction time (min), and pH they remain valuable for assessing the overall efficiency and practical applicability of different photocatalytic systems in water purification. As shown in Table 1, a wide range of synthesis approaches, including hydrothermal, solvothermal, sol–gel, and impregnation–precipitation methods, have been employed to fabricate photocatalysts with diverse morphologies such as nanoparticles, porous structures, rod-like architectures, and spherical grains. These structural differences significantly influence the photocatalytic activity by affecting surface area, light absorption, and charge carrier dynamics.

Table 3.
Summary Table of Photocatalysts for Degradation.

Material	Synthesis Method	Morphology	Degradation Rate (min^{-1})	Light source	Reference
$NiWO_4/CoWO_4$	hydrothermal	porous	0.019 min^{-1}	UV light	[24]
$Cu_2O/WO_3/TiO_2$	hydrothermal	nanoparticles	0.044 min^{-1}	150W Xenon lamp	[25]
Zeolite/Fe_3O_4/CuS/$CuWO_4$	hydrothermal	nanoparticles covering a porous surface structure	0.049 min^{-1}	Sunlight	[22]
Bi_2WO_6-CNP-TiO_2 NTA	solvothermal	rod-like structures	0.0024 min^{-1}	LCS-100 W solar simulator	[26]
CFA/GO/WO_3NRs + Pb^{2+}	hydrothermal	netlike balls	0.015 min^{-1}	250 HW lamp, visible light	[27]
Cu@$ZnWO_4$-K	impregnation-precipitation method	spherical grains	0.015 min^{-1}	Sunlight	[28]
FMMWCNTs@GLYMO@WO_3	hydrothermal	nanoparticles	0.019 min^{-1}	170W Citizen COB LED lamp, visible light	[29]
In-WO_3/rGO	solvothermal	spherical nanoparticles	0.014 min^{-1}	visible light	[30]
$WO_3/TiO_2/SiO_2$	sol-gel	agglomerated spherical nanoparticles	0.012 min^{-1}	Xenon lamp, UV-VIS light	[31]
WO_3 nanopowders	hydrothermal	nanoplate-like particles	0.025 min^{-1}	UV-visible light	This work

Notably, the WO_3 nanopowders synthesized in this work via the hydrothermal method exhibit a degradation rate of 0.025 min^{-1} under UV–visible light irradiation, which is competitive with or superior to many previously reported systems. This enhanced performance can be attributed to their nanoplate-like morphology, which likely provides an increased active surface area and facilitates efficient charge separation. Overall, the comparative analysis highlights that the developed WO_3 nanopowders demonstrate promising photocatalytic activity for paracetamol degradation and can be considered as an effective candidate for environmental remediation applications.

Conclusion

In this work, WO_3 nanopowders were successfully synthesized via a hydrothermal method and evaluated as photocatalysts for the degradation of paracetamol under UV–visible light irradiation. SEM analysis revealed a hierarchical micro/nanostructured morphology composed of well-defined nanoplate-like particles with lateral dimensions of approximately 80–150 nm, while Raman spectroscopy and XRD confirmed the formation of a single-phase monoclinic WO_3 structure with high crystallinity. The optical band gap, determined from Tauc plot analysis, was estimated at approximately 2.9 eV, indicating the ability of WO_3 to absorb near-UV and partial visible light. Photocatalytic experiments demonstrated the progressive decomposition of paracetamol monitored by the

attenuation of the characteristic absorption peak at 243 nm. The degradation process followed pseudo-first-order kinetics according to the Langmuir–Hinshelwood model, yielding an apparent rate constant of $k_{app} = 2.54 \times 10^{-2}$ min $^{-1}$ with a high correlation coefficient ($R^2 = 0.979$). The observed photocatalytic activity is attributed to the developed surface morphology, which enhances light harvesting and provides a large number of accessible active sites, as well as to the presence of defect states that promote charge carrier separation. Comparative analysis with previously reported WO_3 -based and composite photocatalytic systems confirmed that the synthesized nanopowders exhibit competitive performance despite the simplicity of the synthesis route and the absence of co-catalysts or composite modification. From an industrial standpoint, the simple and scalable hydrothermal synthesis employed here makes WO_3 nanopowders attractive for large-scale photocatalyst production. Their proven activity in pharmaceutical pollutant degradation underscores their potential for wastewater treatment and environmental remediation, contributing to the advancement of sustainable water purification technologies.

Acknowledgement

The authors are grateful for the Committee of Science of the Ministry of Science and Higher Education of the Republic of Kazakhstan (Grant No. BR27197639).

References

[1] A. Abdelhaleem al., J. Clean. Prod. **379** (2022) 134571. [*CrossRef*]
[2] H. Dhibi et al., Journal of Water Process Engineering **53** (2023) 103648. [*CrossRef*]
[3] L. Dufner et al., Open Ceramics **18** (2024) 100599. [*CrossRef*]
[4] F. Bozheyev et al., ACS Catal. **15** (2025) 16449–16462. [*CrossRef*]
[5] S. Ghali et al., J. Photochem. Photobiol. A Chem. **446** (2024) 115121. [*CrossRef*]
[6] D.C.S. Gloria et al., Mater. Chem. Phys. **305** (2023) 127947. [*CrossRef*]
[7] A.G. Badillo Morales et al., SSRN (2026). [*CrossRef*]
[8] D. Guettala, H. Gaffour, Reaction Kinetics, Mechanisms and Catalysis **138** (2025) 533–550. [*CrossRef*]
[9] A.H. Shah, M.A. Rather, Environmental Science and Pollution Research **30** (2023) 93916–93933. [*CrossRef*]
[10] P.H. Palharim et al., The Journal of Physical Chemistry C **128** (2024) 20042–20052. [*CrossRef*]
[11] A. Markhabayeva, Physical Sciences and Technology **10** (2023) 33–39. [*CrossRef*]
[12] M.S. Ghasemzadeh, A. Ahmadpour, Environmental Science and Pollution Research **31** (2024) 49059–49078. [*CrossRef*]
[13] M. Moradi, R.A. Sene, F. Rahmani, M. Rezakazemi, Environmental Science and Pollution Research **30** (2023) 99675–99693. [*CrossRef*]

[14] A.A. Adesibikan, O.O. Saliu, P.G. Ndungu, Journal of Water Process Engineering **77** (2025) 108349. [*CrossRef*]
[15] T.T.T. Le et al., Appl. Surf. Sci. **700** (2025) 163253. [*CrossRef*]
[16] R. Hatel et al., Colloids Surf. A Physicochem. Eng. Asp. **711** (2025) 136395. [*CrossRef*]
[17] G. Dhanraj et al., Ceram. Int. **51** (2025) 15030–15042. [*CrossRef*]
[18] A. Gupta et al., Ceram. Int. **51** (2025) 61784–61793. [*CrossRef*]
[19] N. Wang et al., Materials Science and Engineering: B **329** (2026) 119437. [*CrossRef*]
[20] M. Stan et al., Synth. Met. **288** (2022) 117117. [*CrossRef*]
[21] B.Ye. Zhumadilov et al., Int. J. Hydrogen Energy **223** (2026) 154356. [*CrossRef*]
[22] A.H. Ali, A.I. Alwared, Solar Energy **290** (2025) 113383. [*CrossRef*]
[23] B. Hazarika, B. Bhattacharjee, Md. Ahmaruzzaman, Inorg. Chem. Commun. **168** (2024) 112960. [*CrossRef*]
[24] F.A. Alharthi et al., Catalysts **13** (2023) 152. [*CrossRef*]
[25] J.H.F. Chau et al., Catal. Commun. **163** (2022) 106396. [*CrossRef*]
[26] N. Mahhumane et al., Nanomaterials **12** (2022) 2467. [*CrossRef*]
[27] E.C. Umejuru, E. Prabakaran, K. Pillay, ACS Omega **6** (2021) 11155–11172. [*CrossRef*]
[28] M.O. Alfred et al., Ceram. Int. **47** (2021) 19220–19233. [*CrossRef*]
[29] M.S. Ghasemzadeh, A. Ahmadpour, Research Square (2024). [*CrossRef*]
[30] M.F. Abou Taleb, M.M. Ibrahim, J. Alloys Compd. **1003** (2024) 175628. [*CrossRef*]
[31] L. Yanyan et al., J. Mol. Liq. **243** (2017) 761–770. [*CrossRef*]